

3D characterization of heat-induced morphological changes of Au nanostars by fast in-situ electron tomography

Hans Vanrompay^{1*}, Eva Bladt^{1*}, Wiebke Albrecht^{1*}, Armand Béch e¹, Marina Zakhozheva², Ana S anchez-Iglesias³, Luis M. Liz-Marz an^{3,4}, Sara Bals^{1†}

¹Electron Microscopy for Materials Science (EMAT), University of Antwerp,

Groenenborgerlaan 171, 2020 Antwerp, Belgium

²DENSsolutions, Informaticalaan 12, 2628ZD Delft, The Netherlands

³Bionanoplasmonics Laboratory, CIC biomaGUNE, Paseo de Miram on 182, 20014 Donostia - San Sebastian, Spain

⁴Ikerbasque, Basque Foundation for Science, 48011 Bilbao, Spain

* These authors contributed equally.

Supplementary – Info

Synthesis

Materials: Hydrogen tetrachloroaurate trihydrate ($\text{HAuCl}_4 \cdot 3 \text{H}_2\text{O}$, $\geq 99.9\%$), trisodium citrate ($\geq 98\%$), hexadecyltrimethylammonium bromide (CTAB, $\geq 99.0\%$), silver nitrate (AgNO_3 , $\geq 99.0\%$), hydrochloric acid (HCl, 37%), L-ascorbic acid (AA, $\geq 99\%$) and sodium borohydride (NaBH_4 , 99%) were purchased from Sigma-Aldrich. Milli-Q water was used in all experiments. All glassware was washed with aqua regia before use.

Synthesis of gold nanostars: Gold NSs were synthesized using surfactant-free method assisted by silver ions¹. A certain volume of 13 nm gold seeds (0.05 mL, $[\text{Au}] = 0.5 \text{ mM}$) prepared by Turkevich method² was added to an aqueous solution (10 mL) containing HAuCl_4 (0.05 mL, 50 mM) and HCl (0.01 mL, 1 M), followed by fast addition of AgNO_3 (0.03 mL, 10 mM) and AA (0.05 mL, 100 mM). After 30 seconds, the sample was centrifuged (3500 rpm, 30 min) and dispersed in water (2.5 mL). For

the preparation of CTAB-functionalized gold NSs, an aqueous CTAB solution (0.1 mL, 100 mM) was added to the as-prepared gold NSs. After 10 min the solution was centrifuged (3500 rpm, 30 min) to remove excess reactants and CTAB, and dispersed in water (2.5 mL). The average diameter (in nm) determined by measuring the dimensions from the TEM images was 85.5 ± 1.2 .

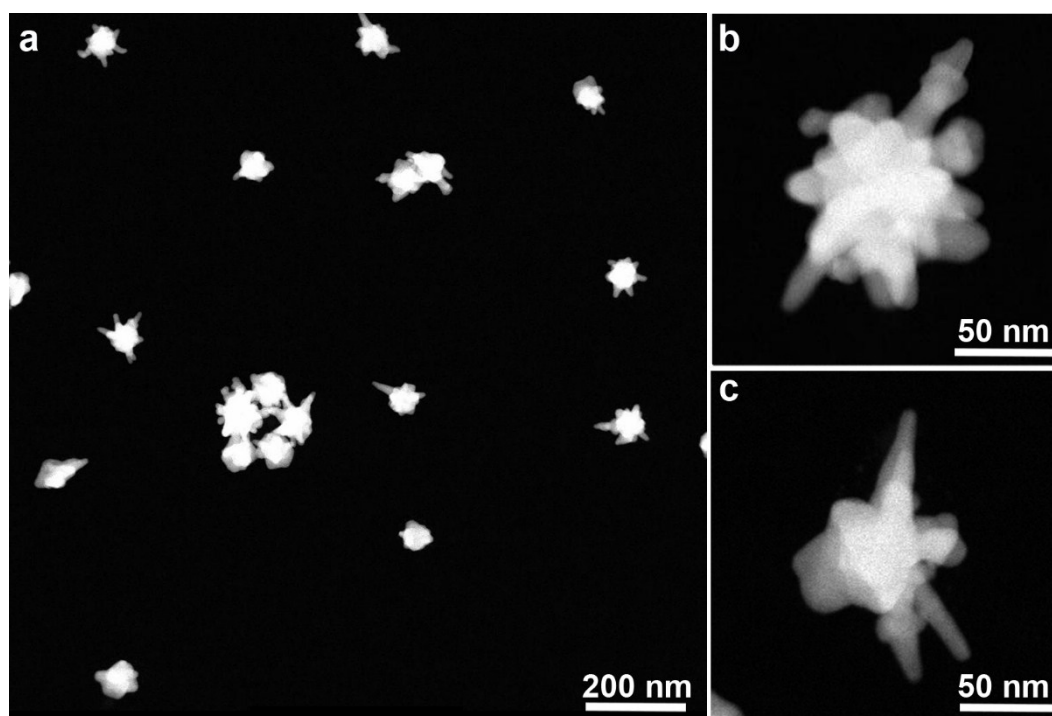


Figure S1. (a) Overview HAADF-STEM image of multiple Au NSs before heating. (b,c) HAADF-STEM images of single NSs.

Electron tomography acquisition and reconstruction

The tilt series for HAADF-STEM tomography were acquired using an aberration-corrected cubed FEI-Titan electron microscope operated at 120 kV (comparison between conventional and fast tomography, Figure 1) and 300 kV (all other data) using a DENSolutions tomography heating holder³ with MEMS-based heating chips⁴. During the fast acquisition, 360 projection images were acquired in 6 minutes time. Owing to the fast acquisition approach, several projection images contained a large defocus value or showed the presence of skewing artefacts in the image due to manual tracking during the acquisition of a frame. Such images were excluded from the complete projection stack. In the remaining images, artefacts originating from mechanical and/or electromagnetic instabilities during the continuous rotation were still present (Figure S2a). These artefacts appeared as a directional band of frequencies in

Fourier space (Figure S2b). Thus, they could be corrected for by applying a low pass filter within Fourier space (Figure S2c), resulting in improved image quality (Figure S2d). After correction of the scanning distortions, we noticed additional distortions due to the fast read-out which caused subsequent projections images to be less similar than expected from the small tilt difference between them (0.37°). These additional distortions were further corrected for by performing non-parametric image registration between a projection image and the average of its three preceding images (Figure S3).^{5,6} Finally, the corrected stack of projection images served as input for 20 iterations of the Expectation Maximization reconstruction (Figure S2b).

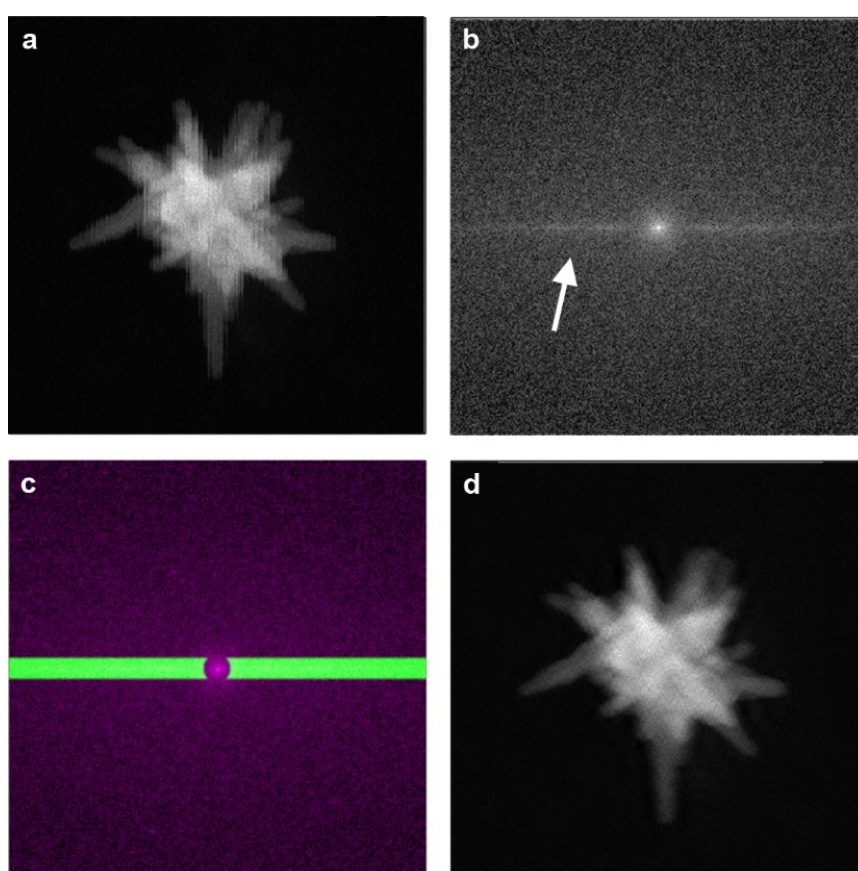


Figure S2. (a) HAADF-STEM image obtained during the fast acquisition of a single NS, revealing noise in the direction of scanning. (b) The amplitude of the Fourier transform of (a). The white arrow indicates the presence of directional noise at higher frequencies. In order to correct the projection images a dedicated low pass filter was used (c) to remove these higher frequencies and restore the projection image (d).

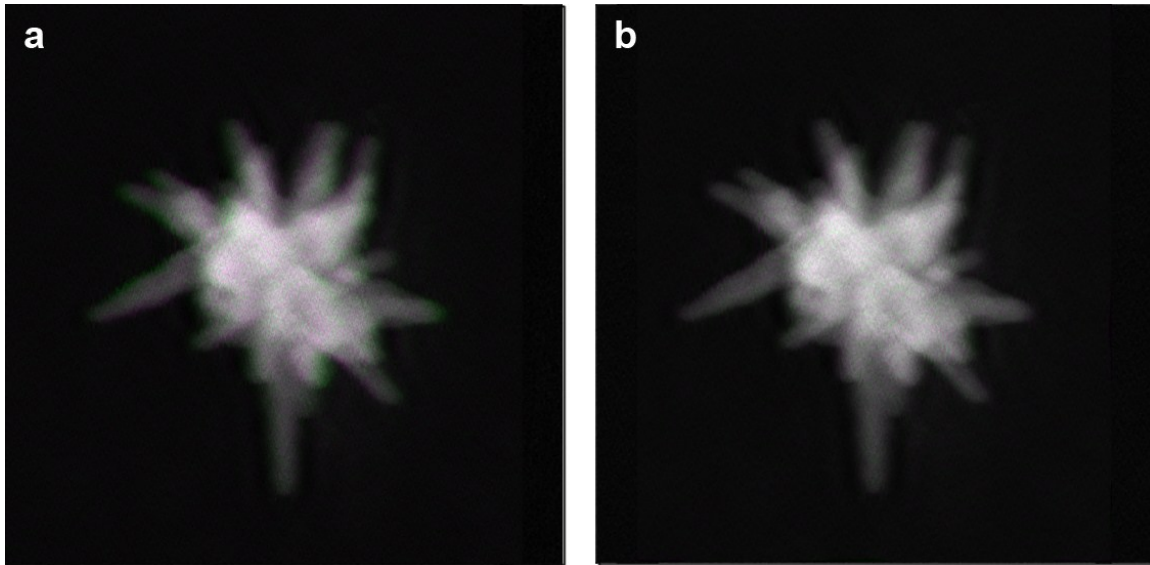


Figure S3. (a) Overlap of two consecutive HAADF-STEM images from the fast acquired tilt series after noise correction showing additional distortions due to fast read-out. One projection image is displayed in green and the other in magenta. (b) Overlap of the same consecutive images from (a) after the non-parametric image registration as described above.

Qualitative and quantitative comparison between fast- and conventional tomography

To validate the fast acquisition approach, a second tomographic series was acquired for one NS using the conventional approach. 75 projection images were acquired over an angular range of $\pm 74^\circ$ with a tilt increment of 2° and intermediate tracking and defocussing. For every projection image, a frame time of 6s was used. Additional focus and repositioning steps lead to a total acquisition time of approximately 1 hour. All other imaging and reconstruction parameters were equal for the conventional and fast acquisition approach. A qualitative comparison of both reconstructions (Figure S4a and b) shows a good visual agreement.

This observation is confirmed by a difference reconstruction (Figure S4c, d). The 3D reconstruction of the conventional acquisition is hereby used as the ground truth and the difference reconstruction was calculated as the difference between the segmented volumes of the two individual reconstructions. The same threshold value was used for the segmentation of both reconstructions, which was chosen based on the histogram of the Expectation Maximization reconstruction of the conventional dataset. Orthoslices through the difference reconstruction show the presence of a thin layer of misclassified

voxels at the outer shell of the NS. The colour within the difference reconstruction indicates whether there is a volume overestimation (white) or underestimation (black) between both datasets. To ensure that the observed differences are not related to alignment imperfections between both reconstructions, their orientations were optimized using intensity based image rigid registration before they were segmented. From Figure S2c and d, a slight deviating orientation between both datasets can be seen, revealing the existence of a slight shear transform on the fast tomographic reconstruction in correspondence to the conventional reconstruction. Nevertheless, as the shear transformation preserves the volume of solid structures and only disorientates the different branches, large differences on our quantitative results are not expected. The origin from these imaging distortions might be related to the fast scanning speed and sample rotation while acquiring a single projection image.

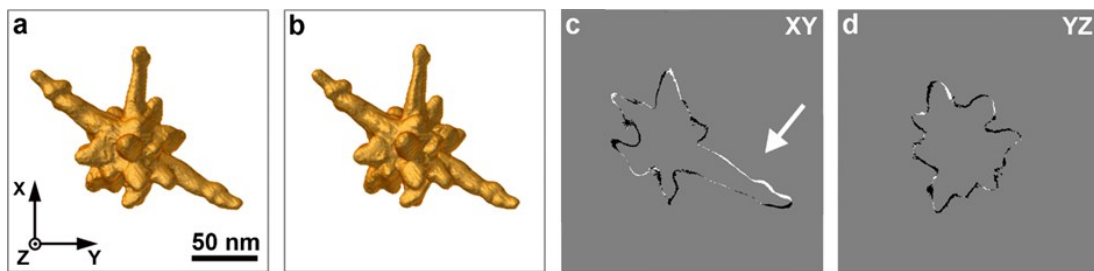


Figure S4. 3D visualisations of the reconstruction (a) based on the conventional acquisition and (b) based on the fast acquisition of the same gold NS. (c, d) XY- and YZ-orthoslices through the difference reconstruction between the conventional and fast acquisition of the same NS are visualized, showing the presence of a thin layer of misclassified voxels. The white/black voxels indicate a volume over/underestimation of the reconstruction related to the fast approach in comparison to the conventional approach.

3D visualizations of an Au NS after different heating times at 300 °C

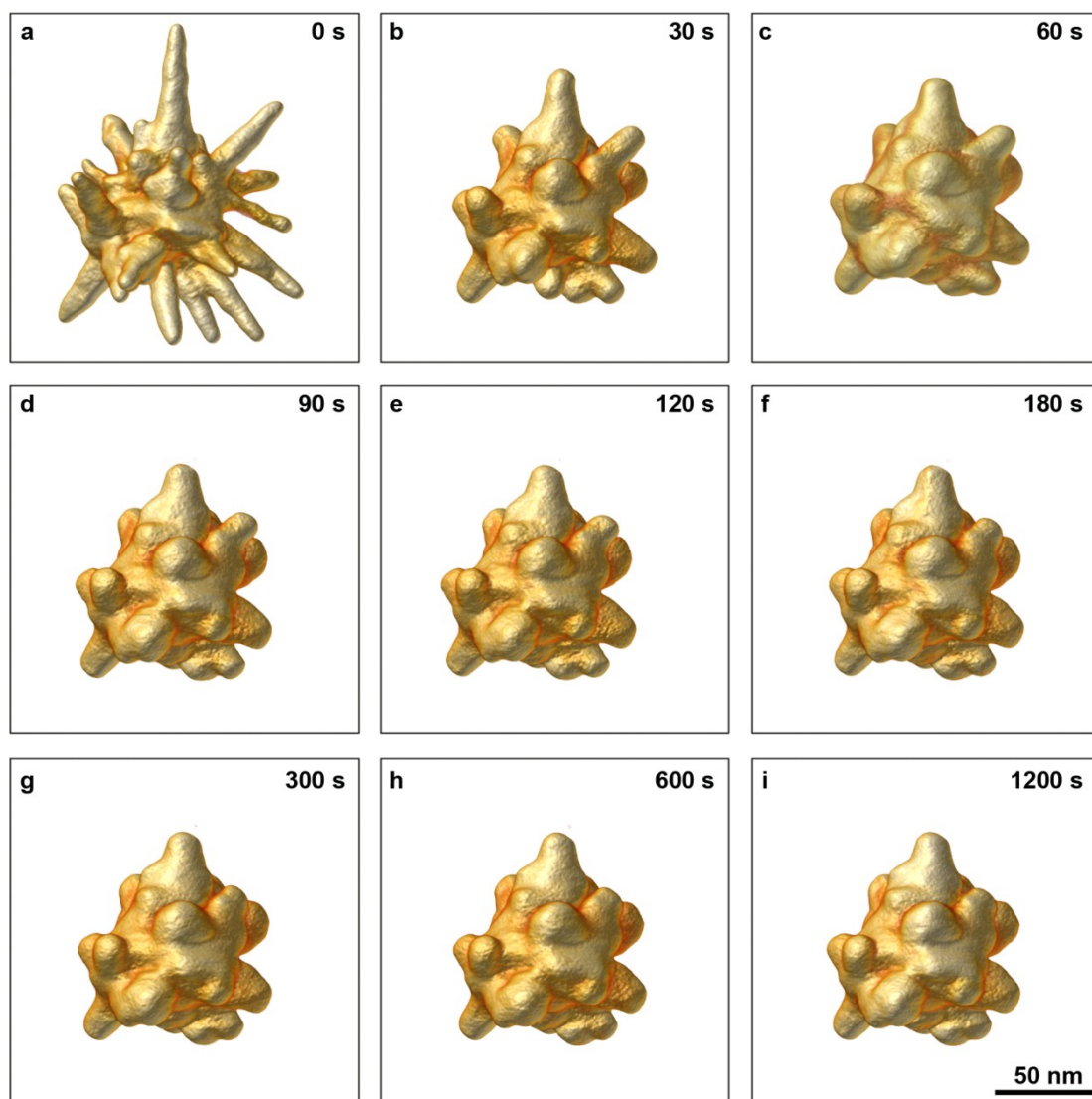


Figure S5. 3D visualisations of the same Au NS after heating at 300 °C for (a) 0 s, (b) 30 s, (c) 60 s, (d) 90 s, (e) 120 s, (f) 180 s, (g) 300 s, (h) 600 s and (i) 1200 s.

3D visualizations of an Au NS after different heating times at 400 °C

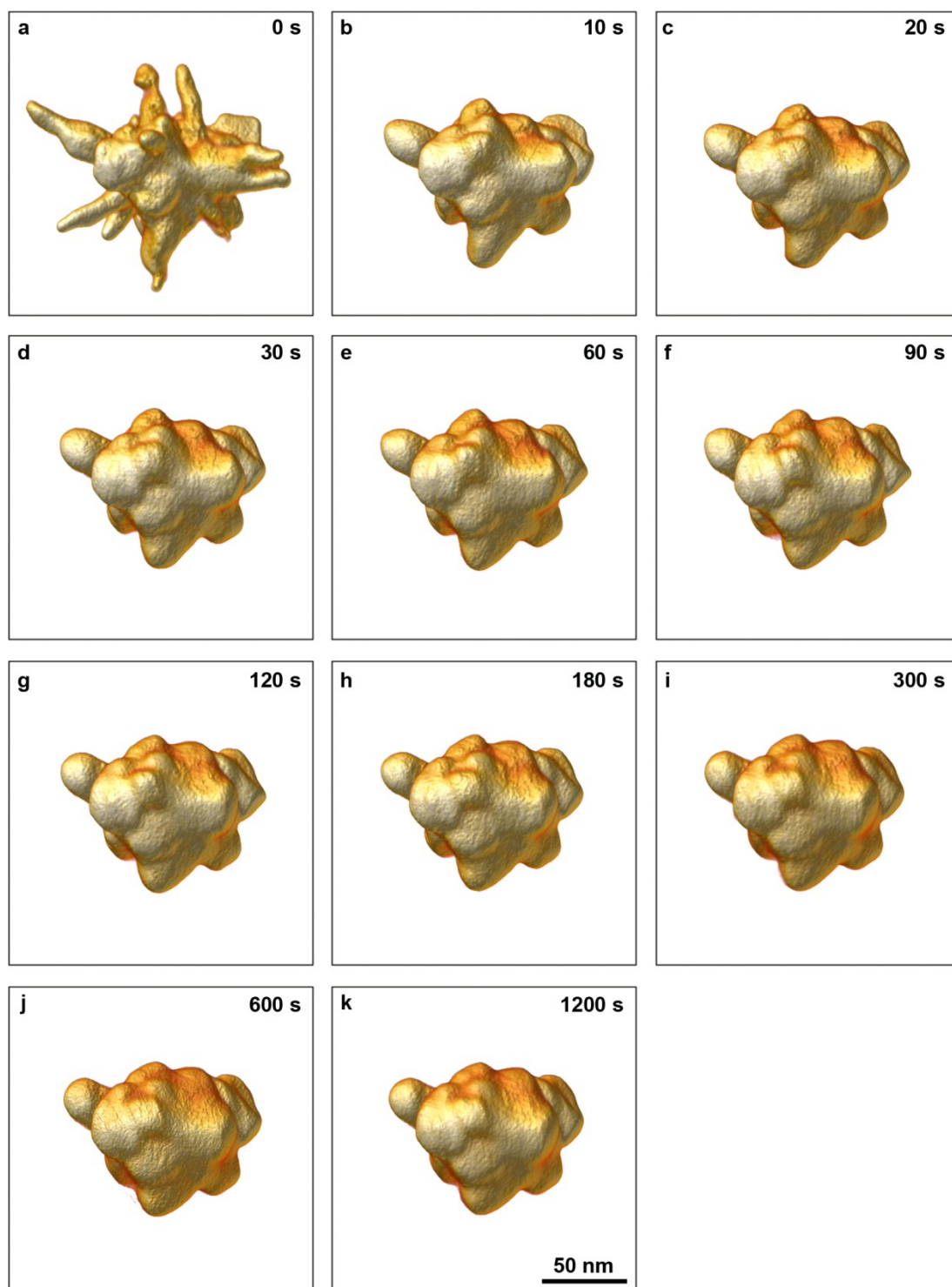


Figure S6. 3D visualisations of the same Au NS after heating at 400 °C for (a) 0 s, (b) 30 s, (c) 60 s, (d) 90 s, (e) 120 s, (f) 180 s, (g) 300 s, (h) 600 s and (i) 1200 s.

Quantitative characterization of the thermal reshaping process

To quantify the redistributed volume (Figure 4) difference reconstructions were calculated by subtracting the segmented reconstructions in successive order. The segmentation threshold was selected based on the assumption that the total volume of the particle remained constant over the course of the experiment. In all cases, the threshold was chosen such that the relative difference in volume between two successive states was below 1%. Since all reconstructions were aligned with respect to each other prior to the difference calculation, remaining discrepancies are directly related to morphological changes occurring during the heating. The range of possible threshold values to achieve a volume difference below 1% was used to determine the accuracy of the quantitative results. By calculating the amount of redistributed volume at the limits of this range, the accuracy on the results was determined as 2.0 %.

The effect of electron beam contamination

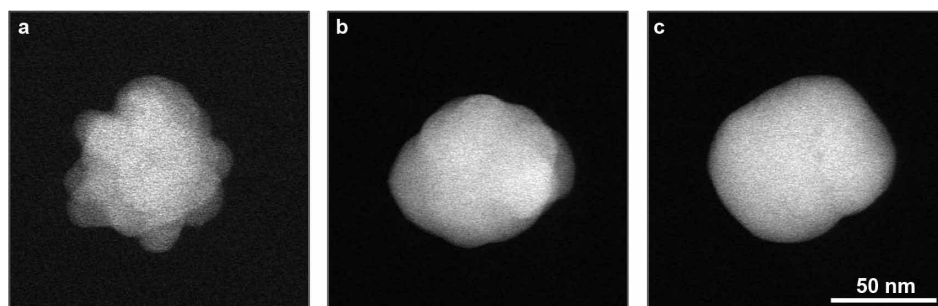


Figure S7. HAADF-STEM images of Au NSs after heating at 400 °C for 1200 s. The NS in (a) was investigated using our fast acquisition approach. The NSs in (b) and (c) were not investigated during heating and only an image after the total heating time was acquired. It can be observed that the NSs in (b) and (c) have a more rounded end morphology.

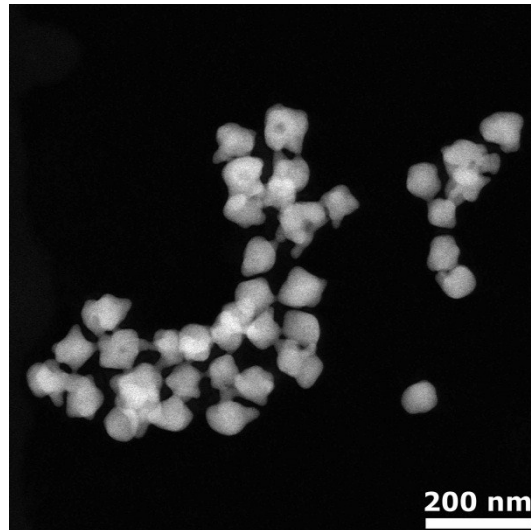


Figure S8. An HAADF-STEM overview image of Au NSs after heating at 200 °C for 1200 s that were not in the field of view during the fast acquisitions of the tilt series.

Boundary Element Method (BEM) simulations

BEM calculations were performed using the MNPBEM Matlab toolbox v14.⁷ The quasi-static approximation was used and the localized surface plasmon resonances were monitored at 150 points in a wavelength range from 500 nm to 1000. A surrounding dielectric constant of 1 was used. The reconstructed NSs were discretized in 6000 vertices using Amira 5.4.0 and used as an input for the BEM simulations. The orientation of the NSs was chosen such that at least one of the nano-branches was aligned with the chosen laser polarization.

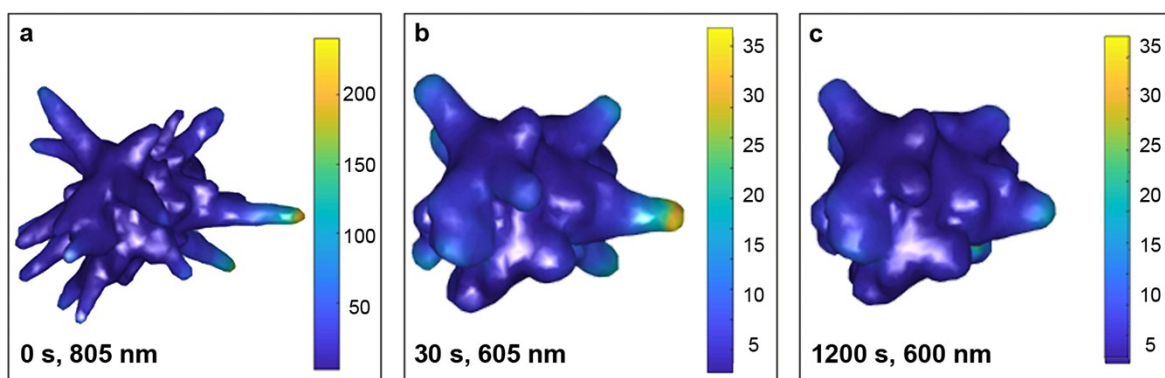


Figure S9. Illustration of electric field enhancement maps at different times during the heating process. The electric field enhancement was plotted for specific wavelengths. Both the time as the chosen wavelength are specified in the bottom left corner of the subfigure. The polarization direction was chosen similar as before, along the axis of the ‘highlighted’ nanobranche.

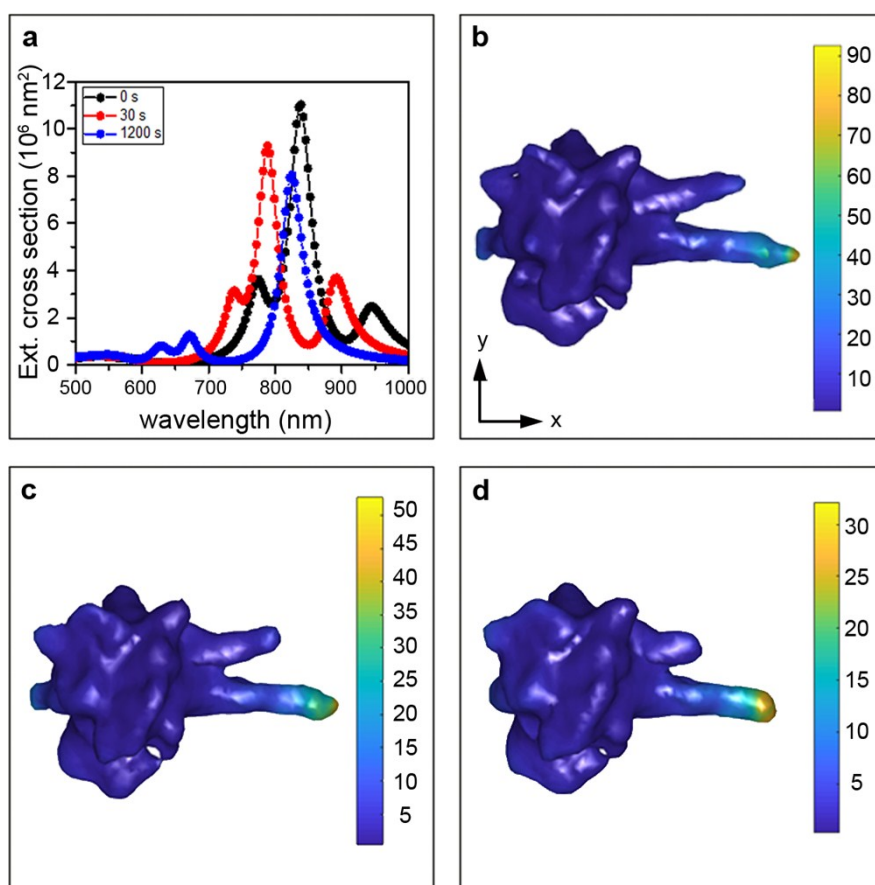


Figure S10. BEM simulations of the Au NS heated at 200 °C performed on a simplified surface deduced of the performed 3D tomographic reconstructions. (a) Extinction cross sections for the unheated and heated nano-branch, after 30 s and 1200 s of heating at 200 °C. (d) Electric field enhancement maps at the different heating times, calculated for illumination over the complete visible spectrum.

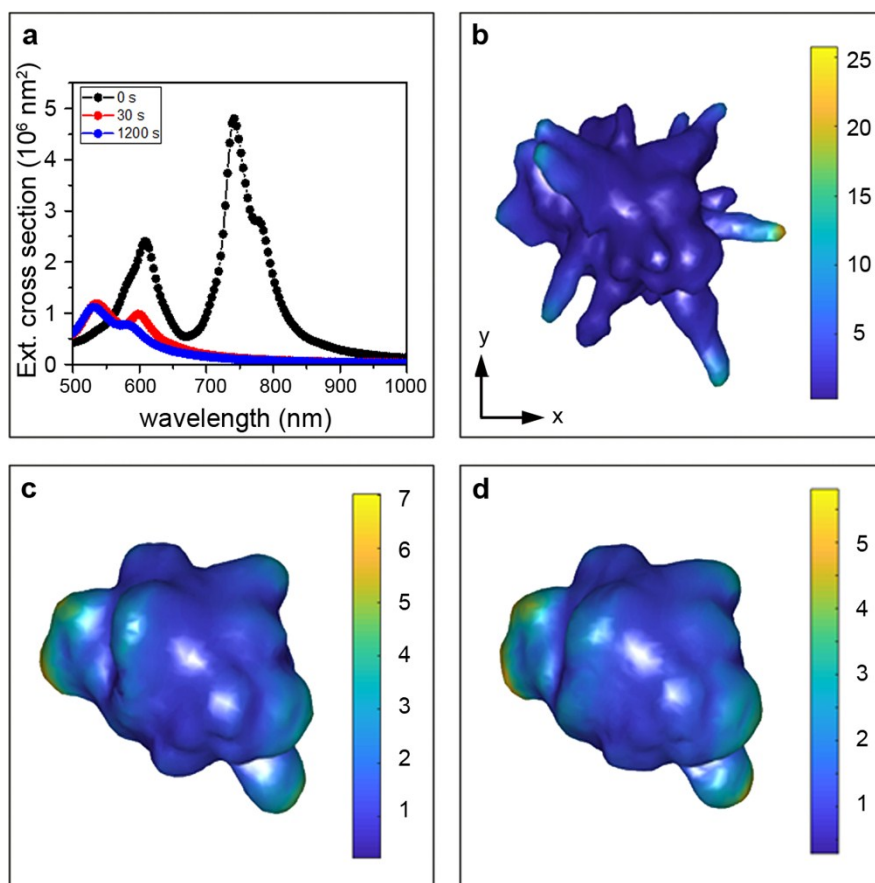


Figure S11. BEM simulations of the Au NS heated at 400 °C performed on a simplified surface deduced of the performed 3D tomographic reconstructions. (a) Extinction cross sections for the unheated and heated nano-branch, after 30 s and 1200 s of heating at 400 °C. (d) Electric field enhancement maps at the different heating times, calculated for illumination over the complete visible spectrum.

References

1. Yuan H, Khoury C, Fales A, Wilson C, Grant G, Vo-Dinh T. Plasmonic gold nanostars: A potential agent for molecular imaging and cancer therapy. *Biomedical Optics and 3-D Imaging*, OSA Technical Digest (Optical Society of America, 2012); paper BM2A.8.
2. Turkevich J, Stevenson PC, Hillier J. A study of the nucleation and growth processes in the synthesis of colloidal gold. *Discuss. Faraday Soc.* 1951;(11):55–75.
3. <https://denssolutions.com/products/wildfire/>
4. <https://denssolutions.com/products/wildfire/nano-chip/>
5. Thirion JP. Image matching as a diffusion process : an analogy with Maxwell ' s demons. *Med. Image Anal.* 1998;2(3):243–60.
6. Vercauteren T, Pennec X, Perchant A, Ayache N. Diffeomorphic demons: efficient non-parametric image registration. *Neuroimage.* 2009;45(1 Suppl):S61-72.
7. Hohenester U, Trügler A. MNPBEM - A Matlab toolbox for the simulation of plasmonic nanoparticles. *Comput Phys Commun.* 2012;183(2):370–81.